

THE AEROSPACE IMAGING INTERFEROMETER ALISEO: FURTHER IMPROVEMENTS OF CALIBRATION METHODS AND ASSESSMENT OF INTERFEROMETER RESPONSE

A. Barducci, F. Castagnoli, G. Castellini, D. Guzzi, P. Marcoionni, *I. Pippi

CNR – IFAC

Via Madonna del Piano 10, 50019 Sesto Fiorentino, ITALY
Tel.: +39 0555226301, Fax: +39 0555226348, *e-mail: I.Pippi@ifac.cnr.it

Commission I, WG-I/6

KEY WORDS: Fourier transform imaging spectrometers, Sagnac interferometer, Optical calibration procedure, Remote sensing, Small-micro satellite.

ABSTRACT:

ALISEO (Aerospace Leap-frog Imaging Stationary Interferometer for Earth Observation) belongs to the stationary interferometers representing a promising architecture for future Earth Observation (EO) sensors due to their simple optical layout. ALISEO has been selected by the Italian Space Agency as the principal payload for a new optical mission based on a micro-satellite (MIOsat). Payloads planned for MIOsat are an extensible telescope, a high-resolution panchromatic camera, a Mach-Zehnder MEMS interferometer, and ALISEO. MIOsat platform is expected to provide the payloads with sight steering capability, in order to mitigate the sensor's data-rate and improve the integration time. ALISEO operates in the common-path Sagnac configuration, and it does not employ any moving part to generate phase delay between the two rays. The sensor acquires the target images modulated by a pattern of autocorrelation functions: a fringe pattern that is fixed with respect to the instrument's field of view. The complete interferogram of each target location is retrieved introducing relative source-observer motion, which allows any image pixels to be observed under different phase delays after moving thorough the sensor's field of view. In this paper we discuss some experimental and theoretical investigations concerning ALISEO's architecture and performance. We describe recent advances in the optical layout selected for the sensor, as well as the outcome of simulations of its main characteristics. In order to refine the calibration of the optical path difference (OPD) of raw interferograms a new data-processing procedure has been developed, based on a set of measurements have been carried out using a double planar diffuser system and several coloured He-Ne lasers. Standard reflectance tiles have been used for validating the wavelength calibration of the instrument, hence proving the reliability of the reflectance retrieving procedure.

1. INTRODUCTION

Our Institute was appointed by the Italian Space Agency (ASI) to carry out a feasibility study to determine the optimal characteristics of a space qualified version of an imaging interferometer to be placed on board of a micro-satellite in a low-cost mission.

A valuable advantage of imaging interferometers is their ability to change the sampled spectral range and their resolving power by simply adjusting the sensor sampling step and the instrument Field-Of-View (FOV) (Harnisch, 2002; Jacquinot, 1954; Griffiths, 1977). An additional advantage is connected with the possible exclusion of the input slit, which strongly reduces the radiant power admitted in dispersive spectrometers. Critical points are associated with the heavy data pre-processing necessary for compensating the instrument response and possible acquisition artefacts (Persky, 1995). Moreover, due to the nature of the acquired interferogram it is crucial adopting detectors with high accuracy of digitalisation (Sellar, 2003).

Our study led to the development of ALISEO (Aerospace Leap-frog Imaging Stationary interferometer for Earth Observation) and ASI selected it as the main payload for the first optical small mission based on a new micro-satellite (MIOsat). Other payloads are a panchromatic camera and a MEMS interferometer for atmospheric sounding. All the

activities related to this space mission have been started on May 2007..

The mission and payload requirements are listed in the tables 1 and 2.

MIOsat operational characteristics	
Orbit	polar, sun-synchronous
Descending node	9:30 - 10:30 a.m. local time
Altitude	500 Km
Expected life-time	2-3 years
Size	1m x 1m x 1m
Mass	Less than 130 Kg
Power	Less than 150 W

Table 1. MIOsat mission characteristics

The paper describes the main characteristics of the prototype imaging interferometer developed at our Institute, moreover some theoretical issues concerning sampling theory in "common path" imaging interferometry are investigated. The procedures for extracting pixel interferograms from a complete set of images and the methods for calibrating the instrument response are presented in section dedicated to Experimental Activity together with some experimental results. Finally the outcomes from our investigation are summarized together with open problems and future work.

ALISEO main characteristics	
Detector	Silicon CCD 2D-array (1024 x 1024 elements)
Spectral range	400 - 1000 nm
Spectral resolution	Better than 5 nm @ 650 nm
Swath	10 Km
FOV	1.15°
Spatial resolution	10 m
Digitalization	12 bit
Expected SNR	200 @ 650 nm
Size	60 cm (along flight direction) x 30 cm (along nadir axis) x 30 cm
Weight	Less than 20 Kg
Power	Less than 25 W

Table 2. ALISEO main characteristics

2.ALISEO INSTRUMENT CONCEPT

ALISEO acquires the image as modulated by a pattern of autocorrelation functions of the energy coming from the observed scene. The complete interferogram of any target locations is observed introducing relative source-observer motion, which allows each pixel to be observed while going across the entire pattern of ElectroMagnetic (EM) autocorrelation function.

The interferometer optical layout is shown in the figure below.

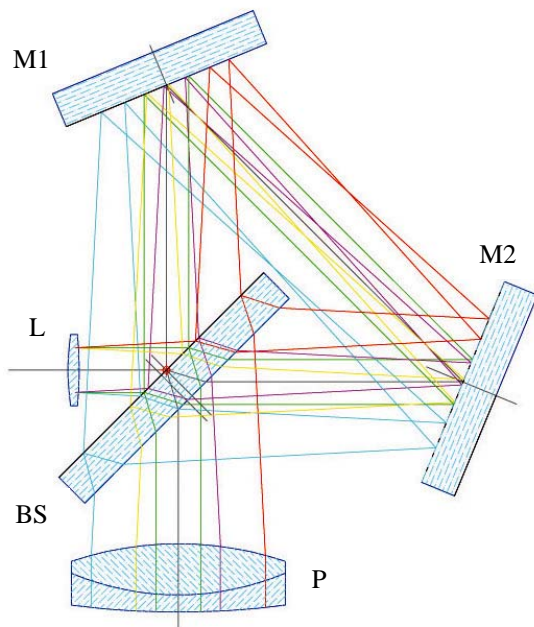


Figure 1. Interferometer Optical layout

Light is collected from the objective L, then the two interfering rays are generated by the beam-splitter BS and travel the triangular ray path in opposite directions by means of two folding mirrors M1 and M2. The two rays are then focused onto the CCD by the camera lens P. It is easy to demonstrate that the BS is the fundamental component, which provides the basic phase-delay between the two coherent rays. Nonetheless, it can be shown that phase-delay is heavily affected by the overall instrument geometry: the BS to M1 and M2 distances and the orientation of the two folding mirrors. Figure 2 shows a picture of the airborne prototype of ALISEO.

This Sagnac interferometer produces a fixed (stationary) pattern of interference fringes of equal thickness (Fizeau fringes). The Optical Path Difference (OPD) between the recombining beams linearly changes with the angle (slope) of the entering ray onto the instrument optical axis.

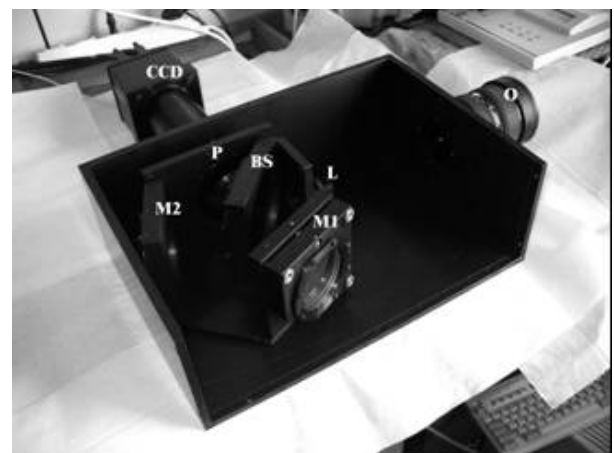


Figure 2: Picture of the inner part of the imaging interferometer developed at our Institute

Due to the absence of entrance slit the device acquires the image of the target superimposed to a fixed pattern of interference fringes. Figure 3 displays a single-frame acquisition of the landscape around Florence (Italy). Due to the low coherence of solar radiation, the fringes visibility (and their number) is limited to a small central region of the collected image. The dark central fringe corresponds to the null optical path difference between the two interfering rays.

Due to the relative sensor-object motion each target's location crosses the entire interference pattern, hence the corresponding pixel is observed under different phase delays when the scene is framed repeatedly in time (Barducci, 2001; Barducci, 2002). In a different wording, the collected image sequence forms a 3-dim array of data (image stack). This data-cube is first processed in order to extract the complete interferogram of every target's point, and then it is cosine inverse transformed to yield a hyperspectral data-cube. Stack geometry is related to important characteristics of sensor and acquired data. As an instance, image sequence and target-sensor relative velocity govern the actual optical path difference between consecutive sample of a retrieved interferogram.



Figure 3: Single-frame acquisition of landscape around Florence city

2.1 Interferogram dispersion

The raw interferogram of the energy coming from a pixel of the observed scene is pre-filtered due to the finite pixel dimension p , and uniformly sampled in a region limited by the detector size D . The measured interferogram $\overline{i(x)}$ may be expressed as:

$$\overline{i(x)} \approx \left[i(OPD(x)) * \text{rect}\left(\frac{x}{p}\right) \right] \text{comb}\left(\frac{x}{p}\right) \text{rect}\left(\frac{x}{D}\right) \quad (1)$$

x being the pixel position. It can be easily shown that the relationship between OPD and the entering ray direction \mathcal{G} is linear, as long as the device FOV is not superior to a few degrees:

$$OPD(\mathcal{G}) = \frac{a}{f}(j - j_0)p = \frac{a}{f}x \quad (2)$$

a being the proportionality constant between OPD and \mathcal{G} , and f the focal plane distance. The constant a is related to the maximum digitised optical path difference OPD_{\max} and to the maximum angle \mathcal{G}_{\max} .

The raw interferogram is constituted by points $(x, DN(x))$, which indicate the pixel position on the detector and the corresponding electronic signal expressed in digital number. According to Shannon's theorem the interferogram sampling frequency k_s should be greater than the full bandwidth k_{\max} of the concerned signal:

$$k_s = \frac{1}{2\delta OPD} \geq k_{\max} \quad (3)$$

In view of Eq.3 the minimum wavelength λ_{\min} we can reconstruct avoiding signal aliasing is $\lambda_{\min} = 2\delta OPD$, δOPD being the optical path difference subtended by two adjacent pixels. Otherwise speaking, the greatest wavenumber (i.e. the shortest wavelength) one can observe without aliasing is that wavelength for which not less than two detector elements cover one fringe cycle. All wavelengths longer than this limit will have their fringe cycles sampled by more than two detector elements.

2.2 Spectrum recovery

As known the spectrum of any pixels have to be reconstructed by means of an inverse cosine transform; i.e. the real part of the inverse Fourier transform. A possible critical point for performing this transformation is constituted by a not perfect knowledge of the factor $\gamma = \frac{a}{f}$, which is essential for

computing the OPD corresponding to a generic position x . As long as some error affects the knowledge of the factor γ the calculated inverse transform will lack of accuracy, possibly originating a wrong estimate of the pixel spectrum. A preliminary issue is allowing some theoretical modelling that can account for this type of uncertainty. Let us suppose that the value $\tilde{\gamma}$ available for the factor γ be erroneous, then the retrieved spectrum $\tilde{I}(k)$ differs from the true one $I(k)$ as stated by the following equations:

$$\tilde{I}(k) = \text{Re} \left\{ \int_{\mathcal{G}} i_{id}(x) e^{2\pi j k \tilde{\gamma} x} dx \right\} \quad (4)$$

$$\tilde{I}(k) = \text{Re} \left\{ \int_{\mathcal{G}} i_{id}(x) e^{2\pi j \tilde{k} x} dx \right\} \quad (5)$$

\tilde{k} being:

$$\tilde{k} = k \frac{\tilde{\gamma}}{\gamma} \Rightarrow \tilde{\lambda} = \lambda \frac{\gamma}{\tilde{\gamma}} \quad (6)$$

It can be easily shown that the:

$$\tilde{I}(k) = I(\tilde{k}) \quad (7)$$

Therefore, an error in the interferogram dispersion gives rise to a corresponding wavelength scale error in the spectrum domain.

Let us note that the difference $I(k) - I(\tilde{k})$ may become large around narrow absorption lines due to the atmosphere or the observed target. A second trouble that can affect the inverse transform procedure is connected with the exact knowledge of the interferogram's centre. It is evident that an error affecting the central position of the interferogram produces a well-known cosine-like modulation of the inverse cosine transform.

3. EXPERIMENTAL ACTIVITY

3.1 Calibration procedure

Preliminary measurements have been carried out in order to calibrate the interferometer response. Two dyed He-Ne lasers ($\lambda^{red} = 632.8nm$ and $\lambda^{green} = 543.2nm$) have been employed for illuminating a double planar diffuser in order to obtain a homogeneous and isotropic radiation distribution inside the instrument FOV. Figure 4 shows a single image-frame obtained with the green laser source. The high number of these interference fringes is related to the high intrinsic coherence-degree of the employed radiation source.

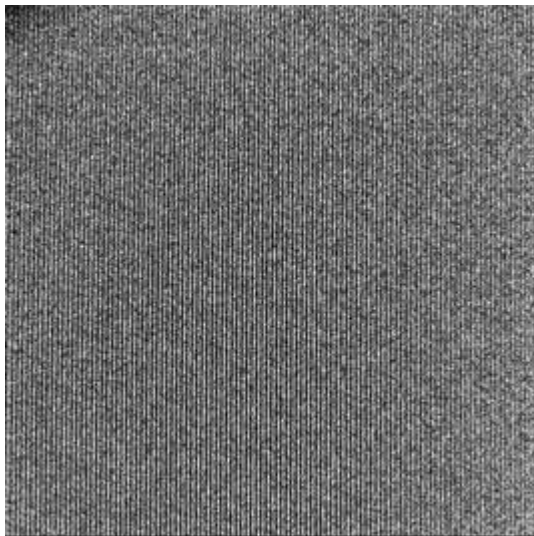


Figure 4: Raw image (grey scale) obtained illuminating a double planar diffuser with a green He-Ne laser. The image is filled with a pattern of across-track interference fringes of equal thickness

The pre-processed interferogram should have a null-mean, starting and ending tails approaching to zero, and any optical artefact removed. In order to achieve these characteristics, we have elaborated a general scheme which is based on the following main steps (Barducci, 2001a):

- dark signal subtraction to account bias and noise in the detector electronic stage;
- instrument spatial response compensation to remove saturated pixels, hot and cold pixels, and fixed-pattern noise;
- geometrical and radiometric distortion correction to remove effects of vignetting and spatial shift of the fringes;
- DC-offset subtraction
- apodization to avoid "Gibbs effect" (ringing phenomenon);
- cosine inverse transform to retrieve the un-calibrated at-sensor radiance spectrum;

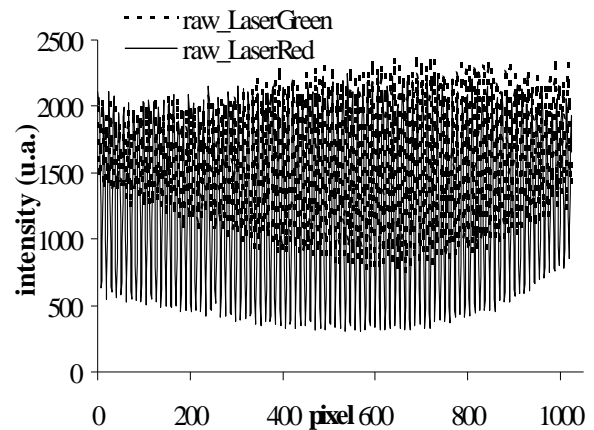


Figure 5. Interferograms averaged over all the columns of image of Figure 3 for the two He-Ne measurements.

The spectral dispersion of optical path differences, which is due to the dispersion law of the refractive index of the beam splitter makes the calibration of the OPD axis really a complex task. When a broad spectral range is exploited, the OPD values may significantly depend upon the spectrum of the observed target. Thus the inversion model of the interferogram as well as the spectral calibration of the sensor might be difficult and their interpretation ambiguous.

The uncalibrated radiance, retrieved applying gaussian apodization are plotted versus wavelengths in Figure 6. Due to the circumstance that the employed spectral source may be approximated to an impulse-like radiation source, this measurement is also a good test to estimate the instrument spectral resolution: roughly 23 nm at 632 nm. Let us note that the spectral resolution has been lowered due to apodization, and OPD spectral dispersion.

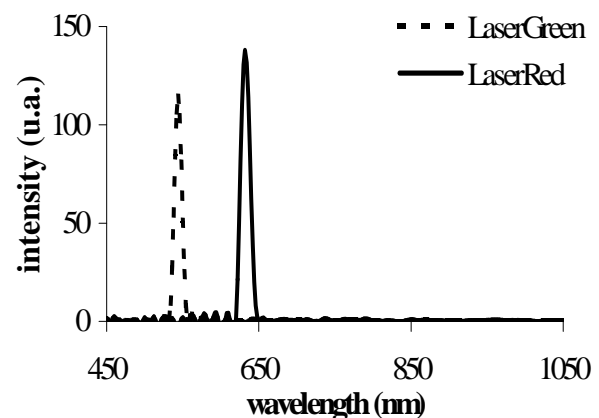


Figure 6. Uncalibrated spectra of at-sensor radiance retrieved by cosine transforming the interferograms plotted in Figure 4.

3.2 SNR estimates

We have executed 40 measurements employing a 600W halogen lamp, each measurement being constituted by 30 frames. The mean and the standard deviation have been computed for each pixel-sample, hence obtaining a set of 1024 mean and standard deviation values interferograms. The SNR

and the noise amplitude have been so estimated, and their plots are shown in Figure 7.

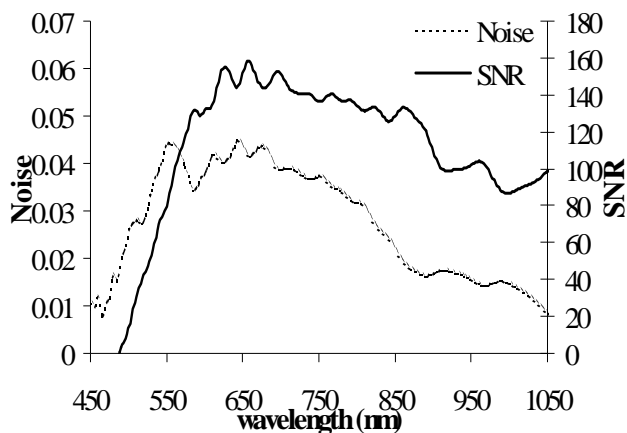


Figure 7: Plot of SNR and noise amplitude (standard deviation) as computed from 40 interferograms collected observing the same radiation source.

2.3 Reflectance spectra reconstruction

Standard reflectance tiles together with diffusers doped with Holmium and Rare Earths have been used to check the reflectance spectra retrieved from ALISEO interferograms. For each tile a complete interferogram has been reconstructed, then the at-sensor radiance have been computed. Reflectance spectra are calculated taking as reference the radiance spectrum extracted from a Spectralon tile. Results of these measurements are plotted in Figure 8.

Retrieved reflectance spectra have been used to verify the wavelength calibration of the instrument. The obtained results are in fair agreement with reference data. We suppose that partial departure of retrieved spectra from references is caused by the still insufficient compensation of the spectral dispersion of OPD.

5. CONCLUSIONS

In this paper an imaging interferometer laboratory prototype of the ALISEO sensor has been presented. The optical layout and the configuration of the instrument have been analysed, and the main differences with existing interferometers have been assessed. A procedure to retrieve the at-sensor radiance has been presented and discussed. Experimental investigation carried out at our Institute allowed us to measure the interferometer spectral resolution and the range of wavelengths that can be reconstructed. Future activities will be devoted to the implementation of a procedure for performing atmospheric corrections of the acquired images on board of an aircraft.

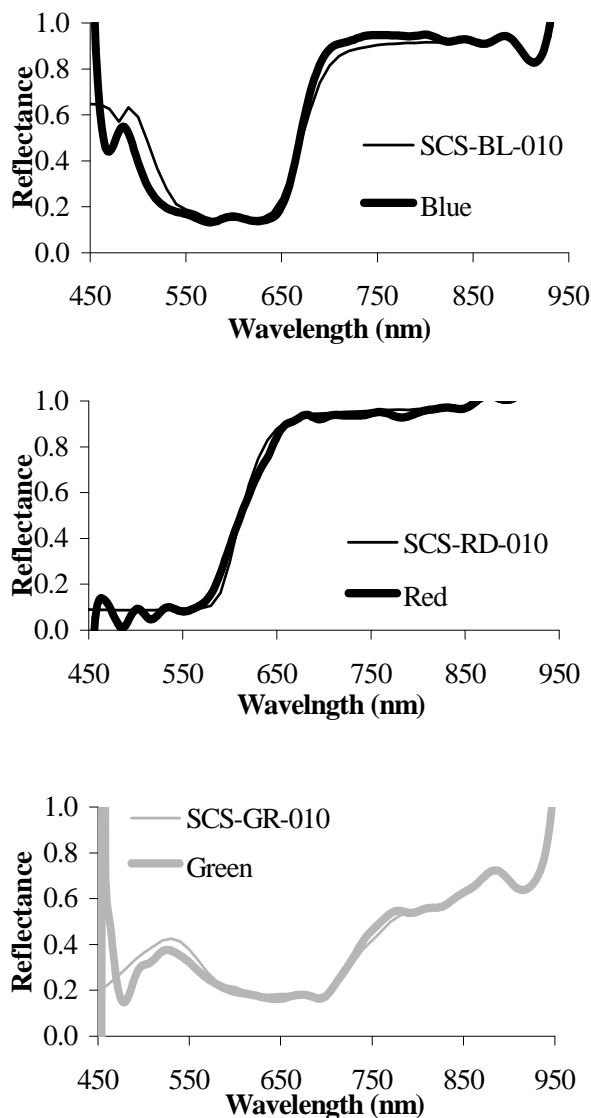


Figure 8: Standard tiles reflectance spectra : reconstructed spectra from measured interferograms are shown with a bold line. Labsphere reflectance spectra are plotted with a thin line.

REFERENCES

- Barducci A., P. Marcoionni, I. Pippi, M. Poggesi, 2001. Simulation of the Performance of a Stationary Imaging Interferometer for High Resolution Monitoring of the Earth, In *Sensors, Systems, and Next-Generation Satellites VII, Proc. SPIE* 4540, pp. 112 – 121.
- Barducci A., I. Pippi, 2001a. Analysis and rejection of systematic disturbances in hyperspectral remotely sensed images of the Earth, *Applied Optics*, 40, pp. 1464 – 1477.
- Barducci A., F. Casini, F. Castagnoli, P. Marcoionni, M. Morandi, I. Pippi, 2002. Performance assessment of a Stationary Interferometer for High-Resolution Remote Sensing, in *Algorithms and Technologies for Multispectral, Hyperspectral, and Ultraspectral Imagery VIII, Proc. SPIE* 4725, pp. 547 – 555.
- Barducci A., P. Marcoionni, I. Pippi, M. Poggesi, 2003. Effects of Light Pollution Revealed During a Nocturne Aerial Survey

by Two Hyperspectral Imagers, *Applied Optics*, 42, pp. 4349 – 4361.

Barducci A., F. Castagnoli, P. Marcoionni, I.Pippi, 2005. The ALISEO instrument: further improvements of calibration methods and assessment of interferometer response, In "*Sensors, Systems, and Next-Generation Satellites XI*", *SPIE* 5978, pp. 1K – 1-10.

Griffiths P.R., H. J. Sloane, and R. W. Hannah, 1977. Interferometers vs Monochromators: separating the optical and digital advantages, *Applied Spectroscopy*, 31, pp. 485 – 495.

Harnisch W. B., E. Hartman, W. Holota, M. Melf, W. Posselt, M. Rost, M. Steiner, H. O. Tittel, W. Weihs, 2002. Compact Fourier Transform Imaging Spectrometer, ESA-CN

14540/00/NL/WK, Proposal No. A.1999-0366-0-1, 1.2.2000 – 31.3.2002.

Jacquinet P., The luminosity of spectrometers with Prisms, Grating, or Fabry-Perot Etalons, *J. Opt. Soc. Am.*, 44, pp. 761 – 765.

Persky, M. J., 1995 A review of spaceborne infrared Fourier transform spectrometers for remote sensing, *Review of Scientific Instruments*, 66, pp. 4763 – 4797.

Sellar, R. G. and G. D. Boreman, 2003. Limiting aspect ratio of Sagnac inteferometers, *Optical Engineering*, 42, pp.3320 – 3325.